iScience

Article

The first interneuron of the mouse visual system is tailored to the natural environment through morphology and electrical coupling

Graphical abstract

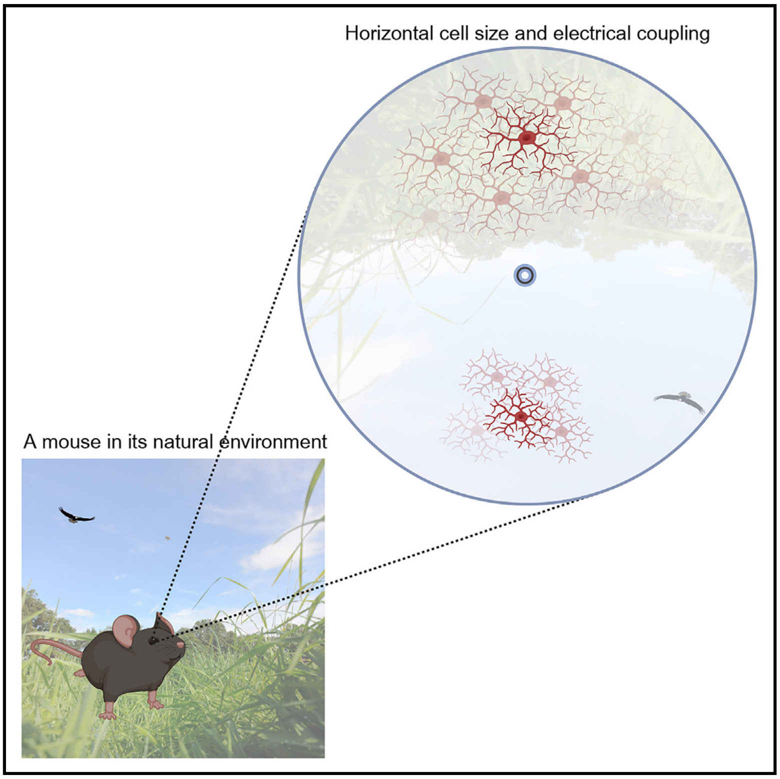

Highlights

- Horizontal cell properties are asymmetrically organized along the dorsoventral axis
- Dorsal cells are larger than ventral cells
- Dorsal cells are more extensively coupled via gap junctions than ventral cells
- Changes occur at the opsin transition zone of photoreceptors, i.e., the visual horizon

Authors

Matteo Spinelli,
Alejandra Acevedo Harnecker,
Christoph T. Block, ...,
Ulrike Janssen-Bienhold, Karin Dedek,
Christian Puller

Correspondence

christian.puller@mpinb.mpg.de

In brief

Biological sciences; Neuroscience; Cellular neuroscience; Sensory neuroscience

Spinelli et al., 2024, iScience *27*, 111276
December 20, 2024
https://doi.org/10.1016/j.isci.2024.111276

CellPress

iScience

CellPress
OPEN ACCESS

Article

The first interneuron of the mouse visual system is tailored to the natural environment through morphology and electrical coupling

Matteo Spinelli,[1,6] Alejandra Acevedo Harnecker,[2,6] Christoph T. Block,[1] Lucia Lindenthal,[1] Fabian Schuhmann,[3] Martin Greschner,[1,4] Ulrike Janssen-Bienhold,[1] Karin Dedek,[2,4] and Christian Puller[1,5,7,*]
[1]Visual Neuroscience, Department of Neuroscience, Carl von Ossietzky Universität Oldenburg, Oldenburg, Germany
[2]Neurosensorics/Animal Navigation, Institute for Biology and Environmental Sciences, Carl von Ossietzky Universität Oldenburg, Oldenburg, Germany
[3]Quantum Biology and Computational Physics, Department of Physics, Carl von Ossietzky Universität Oldenburg, Oldenburg, Germany
[4]Research Center Neurosensory Science, University of Oldenburg, Oldenburg, Germany
[5]Department of Computational Neuroethology, Max Planck Institute for Neurobiology of Behavior – caesar, Bonn, Germany
[6]These authors contributed equally
[7]Lead contact
*Correspondence: christian.puller@mpinb.mpg.de
https://doi.org/10.1016/j.isci.2024.111276

SUMMARY

The topographic complexity of the mouse retina has long been underestimated. However, functional gradients exist, which reflect the non-uniform statistics of the visual environment. Horizontal cells are the first visual interneurons that shape the receptive fields of down-stream neurons. We asked whether regional specializations are present in terms of horizontal cell density distributions, morphological properties, localization of gap junction proteins, and the spatial extent of electrical coupling. These key features were asymmetrically organized along the dorsoventral axis. Dorsal cells were less densely distributed, had larger dendritic trees, and electrical coupling was more extensive than in ventral cells. The steepest change occurred at the visual horizon. Our results show that the cellular and synaptic organization of the mouse visual system are adapted to the visual environment at the earliest possible level and that horizontal cells are suited to form the substrate for the global gradient of ganglion cell receptive fields.

INTRODUCTION

The topographic organization of neurons in the vertebrate retina reflects the lifestyle and behavior of a given species in its corresponding habitat. Some of the most basic functions of the visual system are supported by distinct cell distributions, such as prey capture or threat detection. One of the most prominent specializations is the human fovea, which provides us with high acuity vision. There, the cell density is extremely high, and the dendritic and corresponding receptive fields of the neurons are accordingly small. Our fovea is only one example of many, as topographic specializations can be found in various other vertebrate species.[1,2]

One of the most commonly used model systems for the early visual system in vertebrates is the mouse retina. There, a well-known topographic specialization is the pattern of opsin expression in cone photoreceptors.[3–5] Green- and UV-sensitive opsins are expressed in a gradient along the dorsoventral axis with a steep transition zone at the visual horizon of the mouse, reflecting the natural scene properties of its environment.[6,7] However, the mouse retina has long been thought to lack any further major topographic variations beyond the distribution of opsins. In line with this simplified anatomical perspective, and due to the lack of better knowledge, functional properties of a given cell type have also been assumed to be the same, or at least very similar, across different retinal regions.

Today it is well known that the mouse retina exhibits many different patterns of topographic variations, some are restricted to distinct cell types, whereas others are more global.[2] For instance, retinal ganglion cells show a distinct global density gradient with many more cells located in the ventral retina, i.e., the upper visual field.[8,9] This is accompanied by complex density arrangements of cells in a type-dependent manner.[9–13] Functional specializations of individual ganglion cells of a given type across different retinal locations go hand in hand with the anatomical ones and are equally complex.[14–18] While some of these functional gradients may be shaped by intrinsic features of ganglion cells,[19,20] regional changes of their response properties typically originate in the presynaptic circuitry. However, topographic variations of cells upstream of retinal ganglion cells are poorly understood.

One of the most outstanding examples of a functional gradient in retinal ganglion cells is the dorsoventral change of their receptive field surround structure in terms of amplitude and spatial extent, with remarkable asymmetries in the vicinity of the visual horizon.[21] The origin of this phenomenon remains unknown. Inhibitory amacrine cell signaling in the inner retina contributes to the formation of ganglion cell receptive field surrounds.[22] Nevertheless, horizontal cells in the outer retina also play a fundamental role in the establishment of the ganglion cell receptive fields, including surround properties.[23–25] Thus, we hypothesized that horizontal cells contribute to the region-dependent changes of ganglion cell receptive fields.

Horizontal cells are the first inhibitory interneurons in the vertebrate visual system and positioned to indirectly modulate ganglion cell response properties via lateral synaptic interactions with photoreceptors and bipolar cells in the outer retina.[26] The spatial extent of lateral interactions is determined by horizontal cell dendritic tree size and extensive electrical coupling of dendrites by gap junctions.[27–30] Our analysis of horizontal cell densities and dendritic field sizes, as well as gap junction distribution and the spatial extent of horizontal cell electrical coupling revealed a topographical organization of these features along the dorsoventral axis of the retina. The most prominent distribution asymmetries occurred at the opsin transition zone, i.e., the mouse visual horizon.

RESULTS

Horizontal cells play a crucial role in shaping the retinal output signals.[23–25] Moreover, horizontal cells may match the ganglion cell receptive field surround properties with the visual environment: the strength and spatial extent increase along the dorsoventral axis of the retina.[21] This change should then be reflected in horizontal cell morphological properties to support signaling at different spatial scales, i.e., large in dorsal retina, small in ventral retina, with a distinct transition zone at the visual horizon. Indeed, some evidence suggests that rodent horizontal cells show a certain level of density variation across retinal regions[31,32] which may affect the sizes of cells. Thus, we analyzed the horizontal cell density distribution in high detail by considering each and every cell body across complete wild-type mouse retinas.

Horizontal cell density and dendritic tree size form a gradient across the retina

Whole-mounted retinas were labeled with antibodies against calbindin (CaBP, Figures 1A and 1B), a common mouse horizontal cell marker.[33] The positions of all immunolabeled horizontal cell bodies were manually marked in a merged microscopic tile scan of the flattened retina (Figure 1C), where each dot indicates the position of a horizontal cell body (17650 ± 1412, $n = 5$ retinas, see Figure S2). The cloverleaf shape of the tissue was reconstructed back into the original, almost hemispherical structure of the eyecup with Retistruct to calculate the densities of cells across the complete retinas.[9,34] The local density was calculated and shown in an azimuthal equal distance projection (Figure 1D). The 3D reconstruction allowed a proper averaging of data across five retinas independent of the relief cuts in the original whole-mounts. The retinas were counterstained with antibodies against the short-wavelength sensitive (S-)opsin to reveal the transition zone of opsin expression as an indicator of the visual horizon on the retina.[5,7,21] The transition zone is represented by lines in Figures 1C–1E (also see Figure 4 for representative microscopic images). Note that the transition zone was located far above the optic disc, but then it crossed the peripheral ends of the lower leaflets in a typical retinal whole-mount preparation (Figure 1C). Future studies of retinal whole-mounts may be informed by these regionalization details and ensure a proper interpretation of data collected from definite positions of the mouse retina.

The horizontal cell density was low in the dorsal retina and high in the ventral retina. The steepest change in this gradient occurred in the area of the S-opsin transition zone. The general pattern of this density distribution closely resembled the density gradient of mouse cone photoreceptors.[5,35]

Like other retinal cell types, horizontal cells form a mosaic across the retina, where the dendritic trees of the cells exhibit a constant overlap.[36–38] Thus, a change in cell density should yield a corresponding change in dendritic field sizes. Individual horizontal cells were dye-injected ($n = 69$) to investigate if the density distribution serves as a direct readout of dendritic field size and to gain further insights into the horizontal cell dendritic field structure across the retina (Figures 1F–1J and S3). Convex hulls that encompassed the dendritic trees of the injected cells were used to measure their dendritic areas. The analysis revealed that horizontal cell dendritic trees located above the transition zone covered a much larger area ($n = 25$, 6165 ± 2357 μm^2) than cells below ($n = 44$, 4633 ± 1196 μm^2), with calculated dendritic field diameters of 87 ± 2 μm or 76 ± 9 μm, respectively (tailed Wilcoxon rank sum $p < 0.01$). A fit to explain the relationship between the cell density and the dendritic area (Figure 1K) predicted a coverage factor of ~5, which is largely in line with previously published results.[37] Horizontal cell morphology is characterized by dense dendritic branching in central parts of the dendritic tree and sparser, less arborized dendrites in the periphery.[39,40] Here, injected cells were traced through the image stacks ($n = 23$, Figure S3). A Sholl analysis[41] was applied to the resulting skeletons to investigate whether this branching pattern of horizontal cells may differ between cells from different locations (Figures 1L and 1M). This was not the case, as the results showed a constant branching pattern across the retina. The homogeneous morphology of horizontal cells across all dorsal and ventral cells in our sample became even more prominent (except for one outlier) when the data were normalized to account for the different sizes of the cells.

Horizontal cell dendritic gap junction density changes at the visual horizon

The shape and size of a dendritic tree of a given retinal neuron is typically one of the major determinants of its functional receptive field. Thus, based on our findings, one would expect to find much larger horizontal cell receptive fields in the dorsal retina relative to those located below the opsin transition zone. On the other hand, horizontal cells are well known to exhibit extensive electrically coupled networks via gap junctions, which have been shown to directly affect the receptive field properties of the cells.[27,29,30] Thus, extensive electrical coupling leads to an increase in the spatial extent of receptive fields and lateral signal spread.

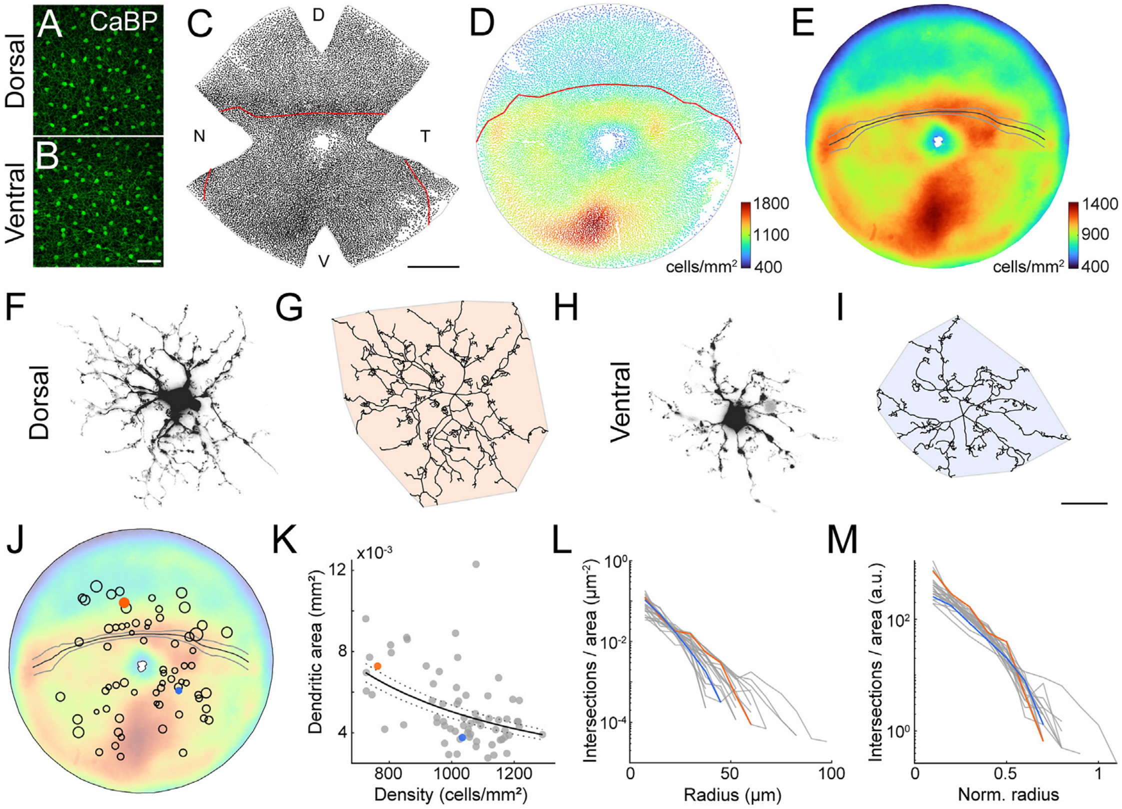

Figure 1. Horizontal cell density and dendritic field size change across the retina

(A and B) Confocal images of dorsal (A) and ventral (B) whole-mounted retina labeled against calbindin (CaBP).

(C) Each dot represents the cell body position of a horizontal cell marked with CaBP across a complete retina of a left eye. The red lines in (C) and (D) mark the S-opsin transition zone (see also Figure 4). D, dorsal; V, ventral; N, nasal; T, temporal.

(D) Azimuthal equal-distance projection of the reconstructed retinal sphere of the data shown in (C). The color of the dots represents the local density of the corresponding cell body position.

(E) Horizontal cell density distribution averaged across 5 retinas. Black line, mean S-opsin transition zone, gray lines, SD ($n = 5$). Color bars in (D) and (E) indicate cells/mm^2.

(F–I) Dye-injected horizontal cells from dorsal (F) and ventral (H) retina, together with the corresponding skeletons (G and I) traced through confocal image stacks of the cell with convex hulls to determine the dendritic tree area.

(J) Positions and dendritic field sizes of 69 injected horizontal cells, superimposed on the averaged density distribution from E. Circle area represents the relative area of the corresponding horizontal cell; for better visibility circles are not shown to scale. Filled orange and blue circles show the positions of horizontal cells from (F) and (H), respectively.

(K) Relation between horizontal cell dendritic field size and local horizontal cell density. Lines describe the best estimate assuming a constant coverage factor (5.04, 95% CI [4.72, 5.37]).

(L) Sholl analysis of dendritic intersections from 23 horizontal cells.

(M) As in (L) but data normalized to dendritic area (convex hull). Scale bars: 50 μm in (B), 1 mm in (C), 20 μm in (I), applies to (F)–(I).

Therefore, we analyzed potential differences of horizontal cell dendritic gap junctions across the retina, which may further influence horizontal cell signaling properties in a region-dependent manner. A prerequisite for such an analysis is, of course, a detailed knowledge of the types and positions of horizontal cell gap junctions. Electrical coupling of mouse horizontal cell dendrites is exclusively supported by gap junctions containing connexin 57 (Cx57).[28,29,42,43] Together with Cx50, Cx57 is also involved in the formation of gap junctions between horizontal cell axon terminals.[44] However, the latter are only connected to rod photoreceptor terminals and do not contribute to dendritic signaling.[45] Therefore, axon terminal connexins were largely excluded from our study by restricting the analysis to mostly dendritic Cx57 in a volume beneath a given cone pedicle base (Figure 2).

Individual dendrites of multiple horizontal cells converge beneath the cone pedicles in the proximal part of the outer plexiform layer (OPL) before their tips invaginate into the pedicle at the glutamate release sites. Mammalian horizontal cells are thought to form dendritic gap junctions primarily in this area of the proximal OPL.[42] Correspondingly, Cx57-immunoreactive plaques were mostly clustered in the proximal OPL beneath the array of cone pedicles (Figures 2A–2C).

Horizontal cells were injected with neurobiotin, a small tracer molecule which can pass through gap junctions between cells

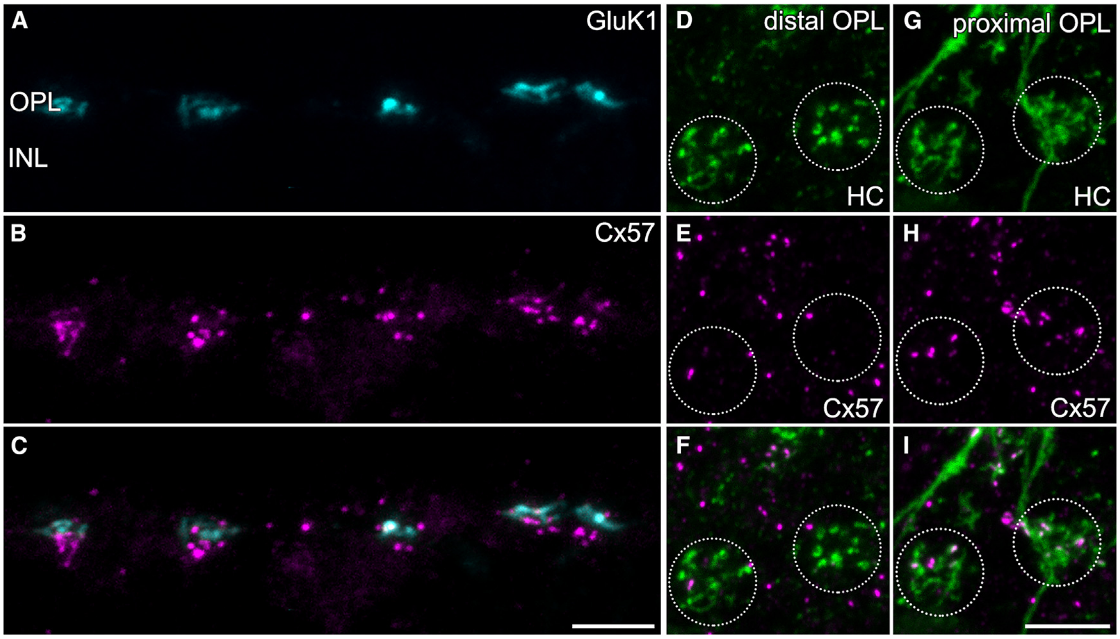

Figure 2. Spatial localization of horizontal cell gap junctions

(A–C) Projections of a confocal image stack of a vertical cryostat section double-labeled for the kainate receptor subunit 1 (GluK1, used as a cone pedicle marker) and the horizontal cell gap junction protein connexin 57 (Cx57).

(D–F) Maximum intensity projections of a confocal image stack of whole-mounted retina labeled with antibodies against Cx57 and with Alexa Fluor 568-conjugated streptavidin after microinjection of neurobiotin into a horizontal cell. The distribution of Cx57 is shown at the tips of horizontal cell (HC) dendrites invaginating into two cone pedicles. Pedicle positions were identified by these clusters of invaginating dendritic tips and are indicated by dashed circles.

(G–I) As in (D) and (F), but ~2 μm beneath the same pedicle position. INL, inner nuclear layer; OPL, outer plexiform layer. Scale bars: 10 μm in (C), applies to (A)–(C); 5 μm in (I), applies to (D)–(I).

to reveal their complete electrically coupled network.[27,30,46,47] Here, we combined neurobiotin-injected cells with immunolabeling of Cx57 and high-resolution fluorescence imaging to reveal the exact position of horizontal cell gap junctions on their dendrites (Figures 2D–2I). Cx57-positive plaques were colocalized with horizontal cell dendrites in a region ~2 μm beneath the pedicle, where the dendrites converged and exhibited slight swellings. This may correspond to a specialized area where glutamate receptor containing desmosome-like junctions are closely associated with gap junctions and the tight-junction protein zonula occludens-1 (ZO-1) on horizontal cell dendrites.[42,48]

Counterstaining of Cx57 with ZO-1 in the dorsal retina (Figures 3A–3H) confirmed previous results where the immunolabeling was largely colocalized beneath mouse cone pedicles.[42] The same experiment performed on the ventral retina yielded a completely different picture (Figures 3I–3P). While the overall extent of GluK1 as a pedicle marker did not obviously change across regions, ZO-1 was less densely clustered and lacked the typical elongated plaques beneath pedicles and in areas between them. Most importantly, the amount of Cx57 immunoreactive puncta appeared largely reduced, resulting in a decrease of colocalization between Cx57 and ZO-1. Next, the distribution pattern of ZO-1 and Cx57 was investigated in detail relative to the S-opsin gradient with its transition zone as an indicator for the visual horizon of the mouse. It became obvious that the change from dense Cx57 clustering and robust colocalization with ZO-1 toward highly reduced Cx57 and the lack of colocalization occurred only within a few hundred microns at the transition zone (Figures 4A–4C). Colocalization of Cx57 with ZO-1 and measurements of the area covered by the corresponding immunostaining was performed in small image stack volumes collected from circular regions of interest (ROIs) beneath each pedicle ("proximal OPL" as in Figures 2G–2I).

The data were collected and pooled from four locations in the dorsal and ventral retina, respectively (example boxes in Figure 4D; 3 retinas, containing a total of 144 ROIs of dorsal pedicles, 131 ROIs of ventral pedicles). The original notion that ZO-1 and specifically Cx57 were less densely clustered at ventral cone pedicles was confirmed by the quantification of immunoreactive areas. These areas were measured within individual ROIs beneath single cone pedicles. Thresholding and normalization was applied (Figures 4E–4G, see STAR Methods section for details) to account for different signal-to-noise ratios of the immunostainings in the 3 retinas. ZO-1 and Cx57-positive areas were reduced from dorsal to ventral retina by 22% and 35%, respectively ($p < 0.001$, Figures 4E and 4F). Furthermore, the colocalization of ZO-1 and Cx57 was reduced by 84% from dorsal to ventral parts of the retina ($p < 0.001$, Figure 4G). No significant differences were observed between the measurements of immunoreactive areas along the nasal-temporal axis (p value Cx57: 0.96, ZO-1: 0.20) or along increasing eccentricities (Cx57: 0.80, ZO-1: 0.64).

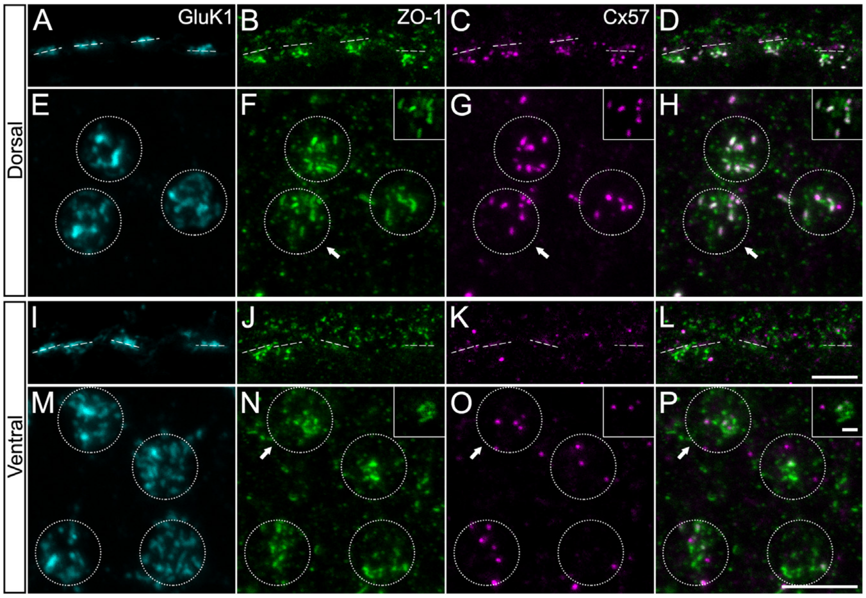

Figure 3. Clustering of ZO-1 and Cx57 differs in dorsal and ventral retina

(A–D) Maximum intensity projections of a confocal stack from a vertical cryostat section of dorsal retina triple-labeled against the kainate receptor subunit 1 (GluK1), the tight junction protein zonula occludens-1 (ZO-1), and connexin 57 (Cx57). Dashed lines indicate pedicle positions marked by GluK1 staining.

(E–H) As in (A)–(D) from a piece of whole-mounted retina. Maximum-intensity projections were chosen to cover the proximal OPL beneath cone pedicles. Circles indicate pedicle positions. Arrows indicate an example pedicle of which single optical sections of the corresponding channels are shown in the box (top right).

(I–P) As in A-H but from ventral retina. Scale bars: 5 μm in (L), applies to (A)–(D) and (I)–(L); 5 μm in (P), applies to (E)–(H) and (M)–(P); 1 μm box in (P), applies for single optical section boxes (F)–(H) and (N)–(P).

As control measurements, colocalization was analyzed again in the same images but with one vertically flipped channel per ROI at single cone pedicles.[49] Colocalization in the flip control of the dorsal retina was significantly reduced by 73%, suggesting that the overlap measured in the original image did not occur randomly. Colocalization in control measurements of the ventral retina was reduced by 45%. This reduction was not significant due to the low amount of colocalization in the original images.

Changes in gap junction organization translates into distinct patterns of electrical coupling

The difference in the gap junction density on horizontal cell dendrites from dorsal and ventral retina was striking. It remained unclear, however, whether this change resulted in a functional difference, i.e., different electrical coupling strengths in dorsal versus ventral regions. Therefore, horizontal cells of wild-type mice were injected with the tracer molecule neurobiotin to visualize the extent of electrical coupling of a given cell in a determined location of dorso- or ventronasal retina (Figure 5A). Beyond the spatial restriction to the nasal retina, each horizontal cell was injected under constant conditions, including current, injection duration, time of day, lighting, and temperature, to allow for proper comparability between the experiments. The results from these experiments confirmed distinct coupling patterns as suggested by our anatomical results. In the dorsal retina, more cells were electrically coupled to a given horizontal cell (n = 7; 233 ± 45 coupled cells) and the coupling extended across a larger area (0.245 ± 0.039 mm^2; Figures 5B–5E). The exact opposite was true for ventral horizontal cells (n = 7), which exhibited coupling to fewer cells (130 ± 46) in a smaller area (0.111 ± 0.047 mm^2).

DISCUSSION

Our study provides evidence for dorsoventral asymmetries of horizontal cell features in the mouse retina, in terms of (1) the cell density and dendritic tree size, (2) the density of gap junctions clustered on their dendrites, and (3) the extent of electrical coupling regarding the number of coupled cells and the area covered by them. Cell density gradients across the mammalian retina are well known, including corresponding morphological changes of the cells.[1,2] It is remarkable, however, that the horizontal cell density gradient reported here is accompanied by a matching change in the synaptic architecture of the cells, i.e., the density and distribution of electrical synapses and the corresponding coupling strength. This change will directly affect the spatial range of signaling at the first synapse in the visual system, as a tight relationship between the extent of electrical coupling and receptive field sizes exists in mammalian horizontal cells.[27,29,30] Moreover, we provide evidence that these asymmetries match the global properties of the visual environment of the animal, where the most prominent transition of the aforementioned horizontal cell features occurs in the area of the visual horizon of the animal.

Horizontal cells support the functional separation of the mouse visual field

Differences in the functional separation of upper and lower mouse visual fields are well known and some neuronal adjustments of the outer retina have already been revealed at the level of photoreceptors and bipolar cells.[3–7,32,50] To our knowledge, horizontal cells have rarely been considered in this context (but see the study by Camerino M.J. et al.[32] their Figure 3). Horizontal cells located above the photoreceptor transition zone receive visual information from the ground, and they possess large dendritic trees and exhibit extensive electrical coupling. Horizontal cells below this zone are positioned for information from the upper visual field by smaller dendritic trees and reduced spatial extent of electrical coupling. Therefore, the characteristics of large dendritic trees paired with extensive coupling versus small dendritic trees paired with reduced coupling operate hand in

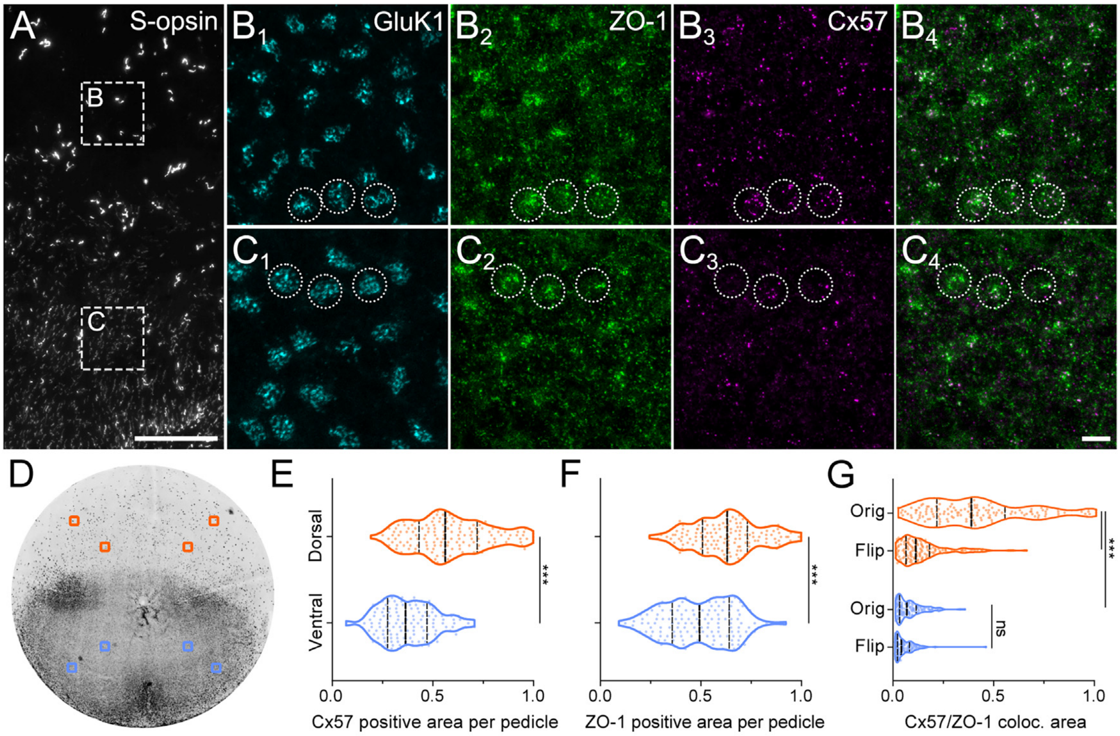

Figure 4. Clustering density of horizontal cell gap junctions changes at the S-opsin transition zone

(A–C) Maximum intensity projections of confocal image stacks from the region of the short-wavelength sensitive (S)-opsin transition zone. The retinal whole-mount was quadruple-labeled with antibodies against S-opsin, GluK1, ZO-1, and Cx57. (A) Cone outer segments positive for S-opsin at the transition zone. Boxes (B) and (C) indicate regions where confocal image stacks (B_1–C_4) were acquired. B_1–B_4 shows GluK1, ZO-1, and Cx57 at the level of the OPL in the position of box B (in A), close to the transition zone but on its dorsal side. Three example pedicles are indicated by circles. C_1–C_4, as in B_1–B_4 but for the area C on the ventral side of the transition zone.

(D) Azimuthal equal-distance projection of tile scans of a complete, whole-mounted retina immunolabeled against S-opsin. Boxes indicate the locations where image stacks were acquired for the quantification of Cx57 and ZO-1 immunostaining.

(E–G) Quantification of the immunolabeled areas (normalized from μm^2) of Cx57 and ZO-1 and their colocalization per circular ROI beneath each pedicle. Measurements were pooled across dorsoperipheral locations (orange, all upper boxes in D combined) and the ventroperipheral locations (blue, all lower boxes in D combined). Dashed lines in violin plots show median and quartiles. Each data point represents the measurement in a ROI beneath one pedicle. Orig, co-localization analyzed in the original image stack, Flip, control measurement where one channel per ROI was vertically flipped. Unpaired, two-tailed Mann Whitney test (E and F) and one-way ANOVA with a post-hoc Tukey test for multiple comparisons (G), ***$p < 0.001$; ns, not significant. Scale bars: 100 μm in (A); 5 μm in C_4, applies to B_1-C_4.

hand as complementary phenomena to create large or small functional units in the lower or upper visual field, respectively (Figure 6). Small functional units can serve high spatial resolution and would be beneficial for the detection of threats from overhead predators, for instance. Previous work has identified the transient OFF alpha ganglion cell as one of the retinal output cell types responsible for triggering innate defensive behaviors upon approach detection.[51–53] These ganglion cells are prominently affected by horizontal cell signaling,[25] which is in line with the idea of horizontal cells contributing directly to the processing of the visual scene and to retinal output signaling. On the other hand, integration of signals across a larger area, specifically in the receptive field surround, may improve signal detection in front of the animal and in the lower visual field assuming more abundant transitions of low and high contrast signals.

The horizontal cell contribution to receptive field properties of mouse ganglion cells in the inner retina has remained a controversial topic, including electrical coupling of horizontal cells, which did not seem to play a dominant role in ganglion cell signaling.[54] However, a series of recent studies from independent research laboratories provided evidence for horizontal cell signaling as a major influence on ganglion cell receptive field surrounds[23–25] with previous inconsistencies in observations likely originating in experimental stimulus properties, such as spatial scales or light levels and the focus on certain ganglion cell types.[25] Therefore, the functional consequences of the horizontal cell feature asymmetries observed here would affect the ganglion cell receptive field surround in the upper visual field to be spatially restricted due to smaller cell sizes and lesser extent of electrical coupling (Figure 6). In the lower visual field, however, the inhibitory feedback signals of horizontal cells distribute across a larger area, causing a much wider surround of postsynaptic cells with potentially lower amplitudes. These ganglion cell receptive field properties have indeed been shown to exist, and they form a gradient across the retina with the most prominent change at the S-opsin transition zone,[21] resembling our findings

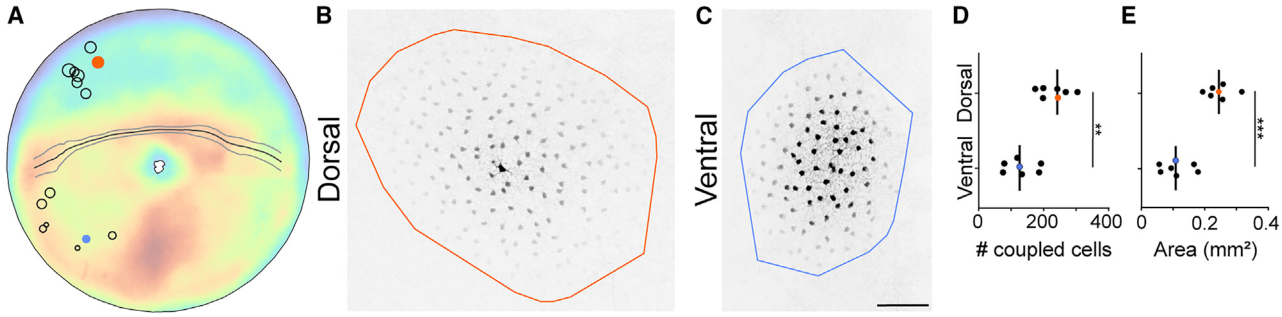

Figure 5. Tracer coupling patterns of horizontal cells differ in dorsal and ventral retina

(A) The position of neurobiotin-injected horizontal cells is indicated by circles superimposed on the density distribution disc taken from Figure 1E. The area of the circles reflects the number of tracer-coupled cell bodies per injected horizontal cell. Orange and blue filled circles represent the example injections in (B)–(E).

(B and C) Example tracer-coupling patterns upon injection of neurobiotin into single cell bodies (B, in dorsal retina; C, ventral). Convex hulls encompassing all neurobiotin-positive cell bodies were used to measure the area of neurobiotin-spread.

(D and E) Quantification of the number of tracer-coupled horizontal cell bodies (D, $p < 0.01$) and the area of tracer-spread (E, $p < 0.001$) per injection (Mann-Whitney tests). Vertical lines indicate median. Scale bar 100 μm in (C), applies to (B) and (C).

of the horizontal cell gradient and its gap junction coupling asymmetry.

The cellular basis of the horizontal cell coupling asymmetry

The cellular basis of the difference in electrical coupling is formed by the asymmetric density distribution of the gap junction protein Cx57 at the horizontal cell dendrites. One cannot rule out that some axonal Cx57 has been included in our measurements, but the numbers should be dominated by dendritic gap junctions because of the restricted analysis areas beneath cone pedicles, where most dendritic gap junctions are formed. Interestingly, our observations included a structural change of gap junctions beneath cone pedicles, beyond a mere reduction of Cx57-positive puncta. This was most prominent in the lack of large, elongated ZO-1 plaques. ZO-1 is typically colocalized or closely associated with dendritic horizontal cell gap junctions, where it is thought to form tight junction barriers at the outer perimeter of gap junction plaques at horizontal cell dendrites but not at their axon terminals.[42] Thus, both of the most prominent protein components at the horizontal cell dendritic gap junction are regulated to meet the demands of the mouse visual environment. The reduction of ZO-1 in the ventral retina was obvious but less striking than the reduction of Cx57. This is likely resulting from the association of ZO-1 with Cx36-containing gap junctions at OFF bipolar cell dendritic tips beneath the cone pedicle[42] combined with an increase in OFF bipolar cell dendritic density in the ventral retina.[32,50] We did not attempt to exclude ZO-1 potentially associated with OFF bipolar cell dendrites from our analysis due to the close spatial vicinity of the two layers of gap junction types.

A compensation of the reduced Cx57 expression by a potential upregulation of another connexin subunit can be ruled out. First, we observed a change in the functional coupling pattern of horizontal cells, which supported the anatomical observations and argued against any compensatory mechanism. Second, Cx50 is another gap junction protein expressed by horizontal cell axons, but it has been shown that it does not compensate for a lack of dendritic Cx57.[44]

Conclusion

Mouse horizontal cells are shaping the ganglion cell receptive field surround properties across a spatial gradient of morphological and functional features, which is adapted to the visual scene of the animal. Future studies are required to elucidate the exact interplay of dendritic tree size and potential modulation of electrical coupling, in concert with the complex local and global modes of horizontal cell signaling features.[40,55] In this context, it would be enticing to analyze horizontal cell features in model species from different habitats and life styles, with natural environments which differ from those of the common C57/Bl6 mouse model in terms of scene statistics and general ecology.

Limitations of the study

We provide evidence for a region-dependent change in the dendritic tree size and electrical coupling of horizontal cells, which likely contributes to the global gradient of ganglion cell receptive fields. However, the possible effects of light adaptation and time of the day have not been explored here. Light adaptation is well known to affect the extent of electrical coupling of horizontal cells via dopamine, which is released by certain amacrine cells, depending on ambient light levels and the circadian rhythm.[56] We kept the light adaptation levels and the time of the experiments (during the subjective day) constant to achieve consistent and comparable results. However, mice are nocturnal animals, and regional coupling patterns at nighttime remain elusive.

RESOURCE AVAILABILITY

Lead contact

Further information and requests for resources and reagents should be directed to and will be fulfilled by the lead contact, Christian Puller, christian.puller@mpinb.mpg.de

Material availability

All unique reagents generated in this study are available from the lead contact with a completed materials transfer agreement.

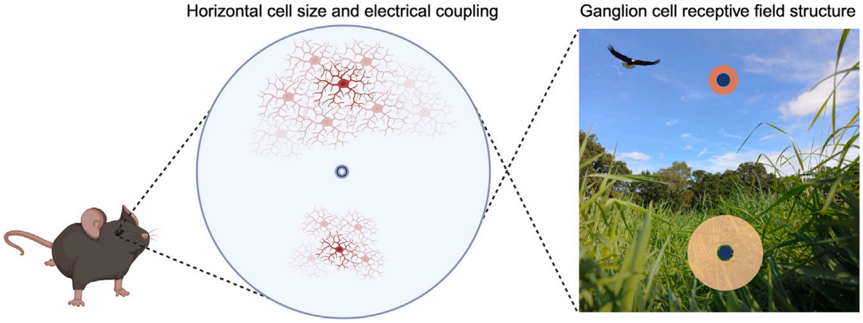

Figure 6. Horizontal cell feature asymmetry supports a receptive field architecture adapted to the visual environment

Dendritic tree size and electrical coupling area of horizontal cells is roughly twice as large in the lower visual field than in the upper. The feature asymmetries shown here are well suited to form the cellular substrate underlying the global asymmetry of ganglion cell receptive field surrounds across the retina (right, brown discs, blue discs represent receptive field centers, adopted from the study by Gupta D. et al.[21]).

Data and code availability

- All data reported in this paper will be shared by the lead contact upon request.
- This paper does not report original code.
- Any additional information required to reanalyze the data reported in this paper is available from the lead contact upon request.

ACKNOWLEDGMENTS

We would like to thank Bettina Kewitz and Hannah Käse for excellent technical assistance, Sabrina Duda for expert support with the acquisition and processing of horizontal cell density data, and Asli Pektaş for help with the large-scale quantification of cells in whole-mounted retinas. We also thank Silke Haverkamp and Ben Reese for valuable comments on an earlier version of the manuscript. We acknowledge the Fluorescence Microscopy Service Unit, Carl von Ossietzky University of Oldenburg, for the use of the imaging facilities. Figure 6 was created with BioRender.com. This work was supported by DFG RTG 1885/2 to M.G., U.J.B., K.D. and DFG SFB1372: Magnetoreception and Navigation in Vertebrates, Project 395940726 to K.D. and M.G.

AUTHOR CONTRIBUTIONS

Conceptualization, U.J.-B., K.D., and C.P.; investigation, M.S., A.A.H., and L.L.; formal analysis, M.S., A.A.H., C.T.B., and F.S., data curation, C.T.B.; writing – original draft, C.P.; writing – review and editing, all authors; supervision, M.G., U.J.-B., K.D., and C.P.

DECLARATION OF INTERESTS

The authors declare no competing interests.

STAR★METHODS

Detailed methods are provided in the online version of this paper and include the following:

- KEY RESOURCES TABLE
- EXPERIMENTAL MODEL AND STUDY PARTICIPANT DETAILS
- METHOD DETAILS
  - ○ Tissue preparations
  - ○ Immunohistochemistry
  - ○ Primary antibodies
  - ○ Retina reconstructions
  - ○ Horizontal cell injections
  - ○ Image acquisition
- QUANTIFICATION AND STATISTICAL ANALYSIS
  - ○ Tracing and morphometric analysis
  - ○ Colocalization analysis
  - ○ Statistical analysis

SUPPLEMENTAL INFORMATION

Supplemental information can be found online at https://doi.org/10.1016/j.isci.2024.111276.

Received: July 15, 2024
Revised: October 2, 2024
Accepted: October 25, 2024
Published: October 28, 2024

REFERENCES

1. Baden, T., Euler, T., and Berens, P. (2020). Understanding the retinal basis of vision across species. Nat. Rev. Neurosci. *21*, 5–20. https://doi.org/10.1038/s41583-019-0242-1.
2. Heukamp, A.S., Warwick, R.A., and Rivlin-Etzion, M. (2020). Topographic Variations in Retinal Encoding of Visual Space. Annu. Rev. Vis. Sci. *6*, 237–259. https://doi.org/10.1146/annurev-vision-121219-081831.
3. Röhlich, P., van Veen, T., and Szél, A. (1994). Two different visual pigments in one retinal cone cell. Neuron *13*, 1159–1166. https://doi.org/10.1016/0896-6273(94)90053-1.
4. Applebury, M.L., Antoch, M.P., Baxter, L.C., Chun, L.L., Falk, J.D., Farhangfar, F., Kage, K., Krzystolik, M.G., Lyass, L.A., and Robbins, J.T. (2000). The murine cone photoreceptor: a single cone type expresses both S and M opsins with retinal spatial patterning. Neuron *27*, 513–523. https://doi.org/10.1016/s0896-6273(00)00062-3.
5. Nadal-Nicolás, F.M., Kunze, V.P., Ball, J.M., Peng, B.T., Krishnan, A., Zhou, G., Dong, L., and Li, W. (2020). True S-cones are concentrated in the ventral mouse retina and wired for color detection in the upper visual field. Elife *9*, e56840. https://doi.org/10.7554/eLife.56840.
6. Baden, T., Schubert, T., Chang, L., Wei, T., Zaichuk, M., Wissinger, B., and Euler, T. (2013). A tale of two retinal domains: near-optimal sampling of achromatic contrasts in natural scenes through asymmetric photoreceptor distribution. Neuron *80*, 1206–1217. https://doi.org/10.1016/j.neuron.2013.09.030.
7. Qiu, Y., Zhao, Z., Klindt, D., Kautzky, M., Szatko, K.P., Schaeffel, F., Rifai, K., Franke, K., Busse, L., and Euler, T. (2021). Natural environment statistics in the upper and lower visual field are reflected in mouse retinal specializations. Curr. Biol. *31*, 3233–3247.e6. https://doi.org/10.1016/j.cub.2021.05.017.
8. Salinas-Navarro, M., Jiménez-López, M., Valiente-Soriano, F.J., Alarcón-Martínez, L., Avilés-Trigueros, M., Mayor, S., Holmes, T., Lund, R.D., Villegas-Pérez, M.P., and Vidal-Sanz, M. (2009). Retinal ganglion cell population in adult albino and pigmented mice: a computerized analysis of the entire population and its spatial distribution. Vis. Res. *49*, 637–647. https://doi.org/10.1016/j.visres.2009.01.010.
9. Duda, S., Block, C.T., Pradhan, D.R., Arzhangnia, Y., Greschner, M., and Puller, C. (2023). Spatial distribution and functional integration of

displaced ipRGCs. Preprint at bioRxiv. https://doi.org/10.1101/2023.09.05.556383.

10. Zhang, Y., Kim, I.-J., Sanes, J.R., and Meister, M. (2012). The most numerous ganglion cell type of the mouse retina is a selective feature detector. Proc. Natl. Acad. Sci. USA *109*, E2391–E2398. https://doi.org/10.1073/pnas.1211547109.
11. Bleckert, A., Schwartz, G.W., Turner, M.H., Rieke, F., and Wong, R.O.L. (2014). Visual space is represented by nonmatching topographies of distinct mouse retinal ganglion cell types. Curr. Biol. *24*, 310–315. https://doi.org/10.1016/j.cub.2013.12.020.
12. Rousso, D.L., Qiao, M., Kagan, R.D., Yamagata, M., Palmiter, R.D., and Sanes, J.R. (2016). Two Pairs of ON and OFF Retinal Ganglion Cells Are Defined by Intersectional Patterns of Transcription Factor Expression. Cell Rep. *15*, 1930–1944. https://doi.org/10.1016/j.celrep.2016.04.069.
13. Berry, M.H., Moldavan, M., Garrett, T., Meadows, M., Cravetchi, O., White, E., Leffler, J., von Gersdorff, H., Wright, K.M., Allen, C.N., and Sivyer, B. (2023). A melanopsin ganglion cell subtype forms a dorsal retinal mosaic projecting to the supraoptic nucleus. Nat. Commun. *14*, 1492. https://doi.org/10.1038/s41467-023-36955-6.
14. Chang, L., Breuninger, T., and Euler, T. (2013). Chromatic coding from cone-type unselective circuits in the mouse retina. Neuron *77*, 559–571. https://doi.org/10.1016/j.neuron.2012.12.012.
15. Sabbah, S., Gemmer, J.A., Bhatia-Lin, A., Manoff, G., Castro, G., Siegel, J.K., Jeffery, N., and Berson, D.M. (2017). A retinal code for motion along the gravitational and body axes. Nature *546*, 492–497. https://doi.org/10.1038/nature22818.
16. Warwick, R.A., Kaushansky, N., Sarid, N., Golan, A., and Rivlin-Etzion, M. (2018). Inhomogeneous Encoding of the Visual Field in the Mouse Retina. Curr. Biol. *28*, 655–665.e3. https://doi.org/10.1016/j.cub.2018.01.016.
17. Holmgren, C.D., Stahr, P., Wallace, D.J., Voit, K.-M., Matheson, E.J., Sawinski, J., Bassetto, G., and Kerr, J.N. (2021). Visual pursuit behavior in mice maintains the pursued prey on the retinal region with least optic flow. Elife *10*, e70838. https://doi.org/10.7554/eLife.70838.
18. Johnson, K.P., Fitzpatrick, M.J., Zhao, L., Wang, B., McCracken, S., Williams, P.R., and Kerschensteiner, D. (2021). Cell-type-specific binocular vision guides predation in mice. Neuron *109*, 1527–1539.e4. https://doi.org/10.1016/j.neuron.2021.03.010.
19. Raghuram, V., Werginz, P., and Fried, S.I. (2019). Scaling of the AIS and Somatodendritic Compartments in α S RGCs. Front. Cell. Neurosci. *13*, 436. https://doi.org/10.3389/fncel.2019.00436.
20. Werginz, P., Raghuram, V., and Fried, S.I. (2020). Tailoring of the axon initial segment shapes the conversion of synaptic inputs into spiking output in OFF-α T retinal ganglion cells. Sci. Adv. *6*, eabb6642. https://doi.org/10.1126/sciadv.abb6642.
21. Gupta, D., Młynarski, W., Sumser, A., Symonova, O., Svatoň, J., and Joesch, M. (2023). Panoramic visual statistics shape retina-wide organization of receptive fields. Nat. Neurosci. *26*, 606–614. https://doi.org/10.1038/s41593-023-01280-0.
22. Diamond, J.S. (2017). Inhibitory Interneurons in the Retina: Types, Circuitry, and Function. Annu. Rev. Vis. Sci. *3*, 1–24. https://doi.org/10.1146/annurev-vision-102016-061345.
23. Chaya, T., Matsumoto, A., Sugita, Y., Watanabe, S., Kuwahara, R., Tachibana, M., and Furukawa, T. (2017). Versatile functional roles of horizontal cells in the retinal circuit. Sci. Rep. *7*, 5540. https://doi.org/10.1038/s41598-017-05543-2.
24. Drinnenberg, A., Franke, F., Morikawa, R.K., Jüttner, J., Hillier, D., Hantz, P., Hierlemann, A., Azeredo da Silveira, R., and Roska, B. (2018). How Diverse Retinal Functions Arise from Feedback at the First Visual Synapse. Neuron *99*, 117–134.e11. https://doi.org/10.1016/j.neuron.2018.06.001.
25. Ströh, S., Puller, C., Swirski, S., Hölzel, M.-B., van der Linde, L.I.S., Segelken, J., Schultz, K., Block, C., Monyer, H., Willecke, K., et al. (2018). Eliminating Glutamatergic Input onto Horizontal Cells Changes the Dynamic Range and Receptive Field Organization of Mouse Retinal Ganglion Cells. J. Neurosci. *38*, 2015–2028. https://doi.org/10.1523/JNEUROSCI.0141-17.2018.
26. Thoreson, W.B., and Mangel, S.C. (2012). Lateral interactions in the outer retina. Prog. Retin. Eye Res. *31*, 407–441. https://doi.org/10.1016/j.preteyeres.2012.04.003.
27. Bloomfield, S.A., Xin, D., and Persky, S.E. (1995). A comparison of receptive field and tracer coupling size of horizontal cells in the rabbit retina. Vis. Neurosci. *12*, 985–999. https://doi.org/10.1017/s0952523800009524.
28. Hombach, S., Janssen-Bienhold, U., Söhl, G., Schubert, T., Büssow, H., Ott, T., Weiler, R., and Willecke, K. (2004). Functional expression of connexin57 in horizontal cells of the mouse retina. Eur. J. Neurosci. *19*, 2633–2640. https://doi.org/10.1111/j.0953-816X.2004.03360.x.
29. Shelley, J., Dedek, K., Schubert, T., Feigenspan, A., Schultz, K., Hombach, S., Willecke, K., and Weiler, R. (2006). Horizontal cell receptive fields are reduced in connexin57-deficient mice. Eur. J. Neurosci. *23*, 3176–3186. https://doi.org/10.1111/j.1460-9568.2006.04848.x.
30. Zhang, A.-J., Jacoby, R., and Wu, S.M. (2011). Light- and dopamine-regulated receptive field plasticity in primate horizontal cells. J. Comp. Neurol. *519*, 2125–2134. https://doi.org/10.1002/cne.22604.
31. Gallego-Ortega, A., Norte-Muñoz, M., Miralles de Imperial-Ollero, J.A., Bernal-Garro, J.M., Valiente-Soriano, F.J., de la Villa Polo, P., Avilés-Trigueros, M., Villegas-Pérez, M.P., and Vidal-Sanz, M. (2020). Functional and morphological alterations in a glaucoma model of acute ocular hypertension. Prog. Brain Res. *256*, 1–29. https://doi.org/10.1016/bs.pbr.2020.07.003.
32. Camerino, M.J., Engerbretson, I.J., Fife, P.A., Reynolds, N.B., Berria, M.H., Doyle, J.R., Clemons, M.R., Gencarella, M.D., Borghuis, B.G., and Fuerst, P.G. (2021). OFF bipolar cell density varies by subtype, eccentricity, and along the dorsal ventral axis in the mouse retina. J. Comp. Neurol. *529*, 1911–1925. https://doi.org/10.1002/cne.25064.
33. Haverkamp, S., and Wässle, H. (2000). Immunocytochemical analysis of the mouse retina. J. Comp. Neurol. *424*, 1–23.
34. Sterratt, D.C., Lyngholm, D., Willshaw, D.J., and Thompson, I.D. (2013). Standard anatomical and visual space for the mouse retina: computational reconstruction and transformation of flattened retinae with the Retistruct package. PLoS Comput. Biol. *9*, e1002921. https://doi.org/10.1371/journal.pcbi.1002921.
35. Ortín-Martínez, A., Nadal-Nicolás, F.M., Jiménez-López, M., Alburquerque-Béjar, J.J., Nieto-López, L., García-Ayuso, D., Villegas-Pérez, M.P., Vidal-Sanz, M., and Agudo-Barriuso, M. (2014). Number and distribution of mouse retinal cone photoreceptors: differences between an albino (Swiss) and a pigmented (C57/BL6) strain. PLoS One *9*, e102392. https://doi.org/10.1371/journal.pone.0102392.
36. Wässle, H., and Riemann, H.J. (1978). The mosaic of nerve cells in the mammalian retina. Proc. R. Soc. Lond. B Biol. Sci. *200*, 441–461. https://doi.org/10.1098/rspb.1978.0026.
37. Reese, B.E., Raven, M.A., and Stagg, S.B. (2005). Afferents and homotypic neighbors regulate horizontal cell morphology, connectivity, and retinal coverage. J. Neurosci. *25*, 2167–2175. https://doi.org/10.1523/JNEUROSCI.4876-04.2005.
38. Keeley, P.W., Eglen, S.J., and Reese, B.E. (2020). From Random to Regular: Variation in the Patterning of Retinal Mosaics. J. Comp. Neurol. *528*, 2135–2160. https://doi.org/10.1002/cne.24880.
39. Raven, M.A., Oh, E.C.T., Swaroop, A., and Reese, B.E. (2007). Afferent Control of Horizontal Cell Morphology Revealed by Genetic Respecification of Rods and Cones. J. Neurosci. *27*, 3540–3547. https://doi.org/10.1523/JNEUROSCI.0372-07.2007.
40. Behrens, C., Yadav, S.C., Korympidou, M.M., Zhang, Y., Haverkamp, S., Irsen, S., Schaedler, A., Lu, X., Liu, Z., Lause, J., et al. (2022). Retinal horizontal cells use different synaptic sites for global feedforward and local feedback signaling. Curr. Biol. *32*, 545–558.e5. https://doi.org/10.1016/j.cub.2021.11.055.

41. Sholl, D.A. (1953). Dendritic organization in the neurons of the visual and motor cortices of the cat. J. Anat. *87*, 387–406.
42. Puller, C., de Sevilla Müller, L.P., Janssen-Bienhold, U., and Haverkamp, S. (2009). ZO-1 and the spatial organization of gap junctions and glutamate receptors in the outer plexiform layer of the mammalian retina. J. Neurosci. Off. J. Soc. Neurosci. *29*, 6266–6275. https://doi.org/10.1523/JNEUROSCI.5867-08.2009.
43. Janssen-Bienhold, U., Trümpler, J., Hilgen, G., Schultz, K., Müller, L.P.D.S., Sonntag, S., Dedek, K., Dirks, P., Willecke, K., and Weiler, R. (2009). Connexin57 is expressed in dendro-dendritic and axo-axonal gap junctions of mouse horizontal cells and its distribution is modulated by light. J. Comp. Neurol. *513*, 363–374. https://doi.org/10.1002/cne.21965.
44. Dorgau, B., Herrling, R., Schultz, K., Greb, H., Segelken, J., Ströh, S., Bolte, P., Weiler, R., Dedek, K., and Janssen-Bienhold, U. (2015). Connexin50 couples axon terminals of mouse horizontal cells by homotypic gap junctions. J. Comp. Neurol. *523*, 2062–2081. https://doi.org/10.1002/cne.23779.
45. Trümpler, J., Dedek, K., Schubert, T., de Sevilla Müller, L.P., Seeliger, M., Humphries, P., Biel, M., and Weiler, R. (2008). Rod and cone contributions to horizontal cell light responses in the mouse retina. J. Neurosci. *28*, 6818–6825. https://doi.org/10.1523/JNEUROSCI.1564-08.2008.
46. Vaney, D.I. (1991). Many diverse types of retinal neurons show tracer coupling when injected with biocytin or Neurobiotin. Neurosci. Lett. *125*, 187–190. https://doi.org/10.1016/0304-3940(91)90024-N.
47. He, S., Weiler, R., and Vaney, D.I. (2000). Endogenous dopaminergic regulation of horizontal cell coupling in the mammalian retina. J. Comp. Neurol. *418*, 33–40. https://doi.org/10.1002/(sici)1096-9861(20000228)418:1<33::aid-cne3>3.0.co;2-j.
48. Haverkamp, S., Grünert, U., and Wässle, H. (2000). The cone pedicle, a complex synapse in the retina. Neuron *27*, 85–95. https://doi.org/10.1016/s0896-6273(00)00011-8.
49. Puller, C., Haverkamp, S., and Grünert, U. (2007). OFF midget bipolar cells in the retina of the marmoset, Callithrix jacchus, express AMPA receptors. J. Comp. Neurol. *502*, 442–454. https://doi.org/10.1002/cne.21315.
50. Sharpe, Z.J., Shehu, A., and Ichinose, T. (2021). Asymmetric Distributions of Achromatic Bipolar Cells in the Mouse Retina. Front. Neuroanat. *15*, 786142. https://doi.org/10.3389/fnana.2021.786142.
51. Münch, T.A., da Silveira, R.A., Siegert, S., Viney, T.J., Awatramani, G.B., and Roska, B. (2009). Approach sensitivity in the retina processed by a multifunctional neural circuit. Nat. Neurosci. *12*, 1308–1316. https://doi.org/10.1038/nn.2389.
52. Kim, T., Shen, N., Hsiang, J.-C., Johnson, K.P., and Kerschensteiner, D. (2020). Dendritic and parallel processing of visual threats in the retina control defensive responses. Sci. Adv. *6*, eabc9920. https://doi.org/10.1126/sciadv.abc9920.
53. Wang, F., Li, E., De, L., Wu, Q., and Zhang, Y. (2021). OFF-transient alpha RGCs mediate looming triggered innate defensive response. Curr. Biol. *31*, 2263–2273.e3. https://doi.org/10.1016/j.cub.2021.03.025.
54. Dedek, K., Pandarinath, C., Alam, N.M., Wellershaus, K., Schubert, T., Willecke, K., Prusky, G.T., Weiler, R., and Nirenberg, S. (2008). Ganglion cell adaptability: does the coupling of horizontal cells play a role? PLoS One *3*, e1714. https://doi.org/10.1371/journal.pone.0001714.
55. Jackman, S.L., Babai, N., Chambers, J.J., Thoreson, W.B., and Kramer, R.H. (2011). A positive feedback synapse from retinal horizontal cells to cone photoreceptors. PLoS Biol. *9*, e1001057. https://doi.org/10.1371/journal.pbio.1001057.
56. Ribelayga, C.P., and O'Brien, J. (2017). Chapter 10 - Circadian and Light-Adaptive Control of Electrical Synaptic Plasticity in the Vertebrate Retina. In Network Functions and Plasticity, J. Jing, ed. (Academic Press), pp. 209–241. https://doi.org/10.1016/B978-0-12-803471-2.00010-2.
57. Schindelin, J., Arganda-Carreras, I., Frise, E., Kaynig, V., Longair, M., Pietzsch, T., Preibisch, S., Rueden, C., Saalfeld, S., Schmid, B., et al. (2012). Fiji: an open-source platform for biological-image analysis. Nat. Methods *9*, 676–682. https://doi.org/10.1038/nmeth.2019.
58. Stabio, M.E., Sondereker, K.B., Haghgou, S.D., Day, B.L., Chidsey, B., Sabbah, S., and Renna, J.M. (2018). A novel map of the mouse eye for orienting retinal topography in anatomical space. J. Comp. Neurol. *526*, 1749–1759. https://doi.org/10.1002/cne.24446.
59. Schmucker, C., and Schaeffel, F. (2004). A paraxial schematic eye model for the growing C57BL/6 mouse. Vis. Res. *44*, 1857–1867. https://doi.org/10.1016/j.visres.2004.03.011.
60. Collins, T.J. (2007). ImageJ for microscopy. Biotechniques *43*, 25–30. https://doi.org/10.2144/000112517.
61. Tetenborg, S., Yadav, S.C., Hormuzdi, S.G., Monyer, H., Janssen-Bienhold, U., and Dedek, K. (2017). Differential distribution of retinal Ca2+/calmodulin-dependent kinase II (CaMKII) isoforms indicates CaMKII-β and-δ as specific elements of electrical synapses made of connexin36 (Cx36). Front. Mol. Neurosci. *10*, 425.

STAR★METHODS

KEY RESOURCES TABLE

REAGENT or RESOURCE	SOURCE	IDENTIFIER
Antibodies		
Rabbit polyclonal anti-Calbindin	Swant	Cat#cb38a; RRID: AB_3107026
Guinea pig polyclonal anti-Connexin57-PGS	This paper	N/A
Guinea pig polyclonal anti-Connexin57-CSM	This paper	N/A
Rabbit polyclonal anti-Connexin57	Hombach et al.[28]	RRID:AB_2490076
Mouse monoclonal anti-GluK1(E−12)	Santa Cruz Biotechnology	Cat#sc393420; RRID:AB_2716684
Goat polyclonal anty-S-opsin	Santa Cruz Biotechnology	Cat#sc14363; RRID:AB_2158332
Mouse monoclonal anti-ZO-1	Zymed	Cat#33–9100: RRID:AB_87181
Rabbit polyclonal anti-ZO-1	Zymed	Cat#61–7300; RRID:AB_138452
Donkey anty-rabbit IgG (H + L) Alexa Fluor 488	Invitrogen	Cat#A-21206; RRID:AB_2535792
Donkey anti-mouse IgG (H + L) Alexa Fluor 568	Invitrogen	Cat#A10037; RRID:AB_11180865
Donkey anty-goat IgG (H + L) Alexa Fluor 647	Invitrogen	Cat#A-21447; RRID:AB_141844
Donkey anty-mouse IgG (H + L) Alexa Fluor 647	Invitrogen	Cat#A-31571; RRID:AB_162542
Donkey anty-goat IgG (H + L) Alexa Fluor 405	Abcam	Cat#ab175664; RRID:AB_2313502
Donkey anty-guinea pig IgG (H + L) CF568	Sigma-Aldrich	Cat#SAB4600469; RRID:AB_2832959
Chemicals, peptides, and recombinant proteins		
Alexa Fluor 568 Hydrazide	Invitrogen	Cat#A10441
Streptavidin, Alexa Fluor 568 Conjugate	Invitrogen	Cat#S-11226
Ames′ Medium	Sigma-Aldrich	Cat#A1420
DAPI	Abcam	Cat#228549
Neurobiotin tracer	Biozol	Cat#SP1120-20
Experimental models: Organisms/strains		
Mouse: C57BL/6J	Tierhaus, Carl von Ossietzky Universität Oldenburg	N/A
Mouse: Cx57$^{LacZ/LacZ}$	Hombach et al.[28]	RRID:IMSR_EM:01644
Software and algorithms		
LAS X Software Leica DM6	Leica Microsystems	RRID:SCR_024857
Fiji	Schindelin et al.[57]	RRID:SCR_002285
GraphPad Prism 7.0	GraphPad Software	RRID:SCR_002798
GraphPad Prism 9.0	GraphPad Software	RRID:SCR_002798
Adobe Photoshop	Adobe	RRID:SCR_014199
Adobe Illustrator	Adobe	RRID:SCR_010279
MATLAB	The MathWorks, Inc.	RRID:SCR_001622
R package Retistruct	Sterratt et al.[33]	N/A

EXPERIMENTAL MODEL AND STUDY PARTICIPANT DETAILS

Only mice were used and no new human participants were recruited for this study. All procedures were performed in accordance with the law on animal protection (*Tierschutzgesetz*) issued by the German Federal Government and approved by the local animal welfare committee. Mice of either sex were used, including the wild-type (C57BL/6J), Cx57$^{lacZ/lacZ}$, and Cx57$^{+/+}$ animals on C57BL/6J genetic background.[28] Wild-type mice were used for all experiments except for the validation of antibody specificity (Figure S1). Animals were housed under standard conditions, including a 12-h light/dark cycle with water and food *ad libitum*.

Mice (ages: 2–4 months for quantification of the horizontal cell (HC) density, 3–5 months for immunohistochemistry, 3–4 months for HC injections) were deeply anesthetized with carbon dioxide and killed by cervical dislocation or decapitation.

METHOD DETAILS

Tissue preparations

After ascertaining the death of the animal, eyes were immediately enucleated and lens and vitreous were removed in a 0.01 M phosphate buffered saline (PBS, pH 7.4) or in a 0.1 M phosphate buffer (PB, pH 7.4). For HC injections, animals have been dark adapted for at least 1 h before they were sacrificed and the subsequent tissue preparation was performed under infrared illumination using night vision goggles (No. G18597, Gutzeit-Gmbh). Retinal dissection was performed in Ames medium (Sigma/Biomol) supplemented with sodium bicarbonate and bubbled with carbogen at 30°C–32°C, pH 7.4. Fixation of the tissues was performed at room temperature (RT). Posterior eyecups were immersion-fixed in initially cold 2–4% paraformaldehyde (PFA) diluted in PBS for 15–20 min. Injected retinas were fixed in 2% PFA diluted in 0.1 M PB for 20 min.

For immunohistochemistry, retinas were cryoprotected after fixation in sucrose solution (30% w/v) overnight at 4°C and then stored at −20°C until use. To keep track of the retinal orientation, the choroid fissures were used to place marking cuts into the tissue.[58] For cryosections, the tissue was then embedded in Tissue-Tek O.C.T. Compound (Sakura Finetek) and sectioned vertically at 20 μm using a Leica CM1860 cryostat. For whole-mounted retinas, four radial relieving cuts were made without compromising the initial marking. Then, the retinas were dissected in PBS or in Ames depending on the following set of experiments. This was performed in a way that the complete retina was preserved, including the most peripheral region (outer marginal zone). Finally, the tissue was mounted on a black nitrocellulose filter membrane (Millipore) with the ganglion cell side up, for immunohistochemistry or cell injections.

Immunohistochemistry

Immunohistochemical labeling was performed by an indirect fluorescence method. Vertical sections were incubated overnight at RT with primary antibodies (*Primary antibodies* table and supplemental information, Figure S1). Three different antibodies against Cx57 were used in this study. They were tested extensively and yielded the same Cx57 staining patterns in the mouse retina as previously published.[28,42,43] Thus, they were used interchangeably in this study. Two of the polyclonal antibodies against C-terminal peptides of mouse Cx57 were newly raised in guinea pigs (Davids Biotechnologie GmbH, Regensburg, Germany). They were termed CSM and PGS (Figure S1), and their amino acid sequences are listed in the *Primary antibodies* table. The specificity of the antibodies was demonstrated by immunostainings in wild-type (WT, Cx57$^{+/+}$) and Cx57-deficient mice (KO, Cx57$^{lacZ/lacZ}$).[28] The common Cx57 immunoreactivity of the two different antibodies was readily observed in wild-type animals following standard protocols (see below) but it was absent in retinal sections of Cx57-deficient mice using the same conditions (Figure S1).

Antibodies were diluted in incubation solutions containing either 5% normal donkey serum (NDS), 1% bovine serum albumin (BSA), 0.5% Triton X-100 in PBS, or 5% Chemiblocker (Millipore) and 0.3% Triton X-100 in Tris-buffered saline (TBS, pH 7.6). Afterward, sections were incubated for 90 min with secondary antibodies diluted in the corresponding incubation solution. Whole-mounted retinas were incubated at RT for 2–3 days in the primary antibody solution containing 5% NDS, 1% BSA, and 1% Triton X-100 in PBS. Secondary donkey antibodies were incubated at RT for 2h or overnight in the same incubation solution. Type and dilution of secondary antibodies was the same for vertical sections and whole-mounts (Alexa Fluor 488, 568, and 647, 1:500, Invitrogen; Alexa Fluor 405, 1:500, Abcam; CF568, 1:500, Sigma).

Retinas where HCs were injected with neurobiotin (see "Horizontal cell injections" below), which were intended for immunostaining of Cx57, were fixed and labeled using the same protocol as described above. Alexa Fluor 568-conjugated streptavidin (1:250, Invitrogen) was used to visualize neurobiotin during the secondary antibody incubation.

Retinas were mounted together with the filter paper on slides in Vectashield (Vector Laboratories). Spacers between glass slides and coverslips were used to avoid squeezing the tissue. Dye-injected specimens were directly mounted on glass slides with Vectashield and coverslipped with spacers as described above. Neurobiotin-injected specimens for the tracer-coupling analysis of HCs were first incubated overnight at 4°C with Alexa Fluor 568-conjugated streptavidin (1:250), diluted in incubation buffer containing 10% NDS, 0.3% Triton X-100 in 0.1 M PB before mounting.

Primary antibodies

Antibody	Host, type	Working dilution	Immunogen	Source, Catalog #
Calbindin	Rabbit, Polyclonal	1:2000	Recombinant rat calbindin D-28k	Swant CB-38A
Cx57	Guinea pig, Polyclonal	1:500(w)/1:100(c)	C-terminal peptide of mouse Cx57 PGSRKASFLSRLMSEK	This study
Cx57	Guinea pig, Polyclonal	1:200(w)/1:100(c)	C-terminal peptide of mouse Cx57 CSMSMILELSSIMKK	This study
Cx57	Rabbit, Polyclonal	1:500	CSMSMILELSSIMKK	Janssen-Bienhold et al., 2009
GluK1	Mouse, Monoclonal	1:2000	aa 869-918 C-terminus of human GluK1	Santa Cruz Biot. sc-393420

(*Continued on next page*)

Continued

Antibody	Host, type	Working dilution	Immunogen	Source, Catalog #
S-opsin	Goat, Polyclonal	1:10000	N-terminus of the of human OPN1SW	Santa Cruz Biot. sc-14363
ZO-1	Mouse, Monoclonal	1:100	aa 334–634 of human recombinant ZO-1	Zymed, 33-9100
ZO-1	Rabbit, Polyclonal	1:100	aa 463–1109 of human zonula occludens-1 cDNA	Zymed, 61-7300

Dilutions used for labeling of cryosections (c) or whole-mounted retinas (w) if different depending on condition.

Retina reconstructions

For the large-scale quantification of HC densities, the merged tile scans of image stacks from whole retinas were used. The R package Retistruct[34] was used to reconstruct the dissected whole-mounts to the spherical cap shape of the intact retina. 3D reconstruction allowed a better estimate especially at the cloverleaf outline and avoided some miscalculation introduced by stress during flattening. In each retina, the tissue outline and the incisions were manually marked. In rare cases of folded, damaged, or missing retinal tissue, the extent of the retina was manually estimated. The rim angle of the reconstructed retina was set to 110° and the radius of the retina to 1.5 mm, as measured from independent cryosections and in accordance with earlier reports.[59] The reconstructed spherical caps were visualized as an azimuthal equal-distance projection. Individual calbindin-positive HC bodies were manually marked using the CellCounter plugin in Fiji, in 5 retinas. The boundary of the short-wavelength sensitive (S-)opsin gradient was manually identified in the same 5 retinas and was represented as mean ± standard deviation (SD, Figures 1, 5, S2, and S3). The local density of horizontal cells was calculated in spherical coordinates by counting the number of cells in a 10° spherical cap. This radius corresponds to an arc length of ~260 μm and a counting disc area of 0.21 mm^2. This counting area was corrected to reflect marked regions where data were unattainable. The average density across different retinas was calculated in a fixed regular grid.

Coverage factor was defined as the number of HCs within the dendritic field of one cell and estimated by multiplication of density and convex hull area. Under the assumption of a constant coverage factor, this relation was fitted in MATLAB using the data shown in Figure 1K.

Horizontal cell injections

Cell nuclei in whole-mounted retinas of wild-type mice were visualized by prior incubation in Ames medium containing 0.3–0.5 μM of DAPI (Abcam) for 60 min at 32°C. Then the retinas were mounted onto black nitrocellulose membrane (see above).

Borosilicate glass electrodes were pulled with a micropipette puller (P-97, Sutter Instrument CO) to obtain sharp electrodes with a resistance between 100 and 200 MΩ. HCs were injected either with a fluorescent dye alone (to analyze the morphology of the cells) or with a mixture of dye and the gap junction tracer molecule neurobiotin (to analyze the electrical coupling).

For fluorescent dye injections, the electrodes were filled with 2 μL of 5 mM of Alexa Fluor 568 hydrazide (Invitrogen, diluted in 200 mM KCl) and backfilled with 10 μL of 200 mM KCl. Epifluorescence light was used to identify DAPI-labeled HC bodies based on their location and their relatively large size. Candidate cell bodies were targeted under visual control with epifluorescence illumination and impaled with sharp electrodes for dye iontophoresis using −0.5 nA square pulses of 500 ms at 1 Hz for 3 min. After injections, the retina was fixed in PFA as described above.

Neurobiotin injections were restricted to the nasal side of a given retina. Electrodes were tip-filled with 3 μL of a 1:1 mixture of 4% neurobiotin (SP1120, Biozol) diluted in 0.1 M Tris buffer (pH 7.3) and 5 mM Alexa Fluor 568 Hydrazide, and back-filled with 10 μL of 200 mM KCl in Tris buffer. The dye was injected as described above for 1–2 min before the current was reversed to inject neurobiotin using +0.5 nA square pulses of 500 ms at 1 Hz for 5 min. Then, a neurobiotin diffusion time of 10 min was granted before fixation. Only a single HC was injected per retina (dorsal $n = 7$, ventral $n = 7$) to provide constant conditions for these experiments to quantify tracer coupling.

Image acquisition

High-resolution fluorescence image stacks were acquired using TC SP8 or TCS SL confocal laser scanning microscopes (Leica). Scanning was performed with 63x/1.32 or with 63x/1.4 oil-immersion objectives and z axis increments between 0.1 and 0.3 μm. The SP8 confocal microscope with either 40x/1.3 or 63x/1.4 oil-immersion objectives was also used to acquire image stacks of HC dendritic trees. Image stacks of the coupled HCs were acquired using a 20x/0.70 oil-immersion objective.

Images of entire whole-mounted retinas were obtained with a Leica DM6B epifluorescence microscope equipped with a motorized stage and a 20x/0.5 air objective. Individual image stacks of a tile scan were automatically stitched together in the microscope software (LAS X, Leica). Overviews of the entire retinas were used for the large-scale quantification of HC density and to keep track of the precise location of the injected horizontal cells (see "retinal reconstruction" section).

Images are presented as single optical sections or as maximum intensity projections of image stacks. Some images were further processed with Fiji[57] using the "subtract background" (rolling ball) plugin and intensities were normalized using the "enhance contrast" plugin with 0.01% saturation. Brightness and contrast of the final images were adjusted using Photoshop (Adobe).

QUANTIFICATION AND STATISTICAL ANALYSIS

Tracing and morphometric analysis

Tracer-coupled HCs were manually counted in Fiji using maximum intensity projections of confocal image stacks. Area measurements were based on convex hulls either encompassing dendritic trees of the HCs (Figure 1) or all neurobiotin-positive cell bodies (Figure 5).

Horizontal cell coupling was studied in 14 retinas and the positions and coupling strength were shown along with the independently measured horizontal cell density. The dendritic area was studied in 69 injected cells from 20 retinas (18 animals, either eye). The area was measured from convex hulls of the manually marked dendritic tree. A Sholl analysis[41] was used to compare the dendritic branching pattern of traced HCs (n = 23) across retinal regions. For this, HC skeletons were traced through image stacks using Amira (Thermo Scientific). The number of intersections of dendritic processes with concentric circles was divided by the area of the respective circle. In Figure 1M, each cell was normalized to equal convex hull area to focus only on the arborization patterns, not on sizes. Cells with overlapping, co-injected cells or any interference from blood vessels, which hindered accurate interpretation, were excluded.

Colocalization analysis

Immunoreactivity of Cx57 and ZO-1 was measured to assess spatial extent and colocalization. Confocal stacks of cone pedicles from the mid-periphery and periphery of dorsal and ventral regions from three retinas were analyzed (see boxed regions in Figure 4). The total extent in z direction was chosen to capture the entire thickness of the ZO-1 cluster beneath a given cone pedicle,[42] which typically included 20–25 consecutive optical sections. For each cone pedicle, a circular region of interest (ROI) with a diameter of 7 μm was selected around the ZO-1 cluster. Background and contrast was adjusted as described above, and a global threshold was independently applied. Colocalization of Cx57 and ZO-1 was analyzed with the ‘‘colocalization highlighter’’ plugin in Fiji (MBF collection[60,61]). Areas of colocalization and areas of individual immunostaining per channel were measured in the same ROIs with the ‘‘analyze particles’’ plugin in Fiji. Colocalization areas smaller than 0.01 μm^2 were excluded from the analysis. Colocalization in images with one vertically flipped channel per ROI at a given cone pedicle position served as control measurements.[49] For the quantification of the individual immunostainings, particles with a size smaller than 0.04 μm^2 were excluded from the analysis. This analysis was applied to 3 retinas. The area measurements were normalized (Figures 4E–4G) to account for differences between the samples regarding staining intensity and the relative background staining levels.

Statistical analysis

The areas of convex hulls that encompassed the dendritic trees of injected cells were compared with a tailed Wilcoxon rank-sum test in MATLAB. Further statistical tests were performed using Prism 9 (GraphPad Software) on normalized ZO-1 and Cx57 immunostaining data (Figure 4). A one-way ANOVA with a post-hoc Tukey test for multiple comparisons was used to compare the colocalized area in the dorsal and ventral retina. Flip controls were used to account for randomly observed colocalization. An unpaired, two-tailed Mann Whitney test was used to compare the immunoreactive areas of Cx57 and ZO-1 between dorsal and ventral measurements. A potential influence of the nasal-temporal axis and increased retinal eccentricity was assessed with a multi-way ANOVA (MATLAB). A p-value <0.025 was considered statistically significant. Quantitative data were obtained from 3 retinas including 144 dorsal pedicles, 131 ventral pedicles presented as median and quartiles.

A Mann-Whitney test (Prism 7, GraphPad Software) was performed to test for statistical significance ($p < 0.05$) between the number of coupled cell bodies and the area covered by them (Figure 5). Quantitative data were obtained from 14 retinas (7 retinas for each dorsal and ventral sides) reported as mean ± SD in the text description and the median is indicated in Figures 5D and 5E.